Nanoscale

Na-ion storage in iron hydroxide phosphate hydrate through a reversible crystalline-to-amorphous phase transition

Journal:	*Nanoscale*
Manuscript ID	NR-ART-03-2020-001922.R1
Article Type:	Paper
Date Submitted by the Author:	18-May-2020
Complete List of Authors:	Henriksen, Christian; University of Southern Denmark, Department of Physics, Chemistry and Pharmacy Karlsen, Martin; University of Southern Denmark, Department of Physics, Chemistry and Pharmacy Jakobsen, Christian; University of Southern Denmark, Department of Physics, Chemistry and Pharmacy Ravnsbæk, Dorthe; University of Southern Denmark, Department of Physics, Chemistry and Pharmacy

ARTICLE

Na-ion storage in iron hydroxide phosphate hydrate through a reversible crystalline-to-amorphous phase transition

Received 00th January 20xx,
Accepted 00th January 20xx

DOI: 10.1039/x0xx00000x

Christian Henriksen,[a] Martin Aaskov Karlsen,[a] Christian Lund Jakobsen,[a] Dorthe Bomholdt Ravnsbæk[a,*]

Iron(III) hydroxide phosphate hydrate $Fe_{1.13}(PO_4)(OH)_{0.39}(H_2O)_{0.61}$ is investigated for the first time as a Na-ion battery cathode, which reveals that the material exhibits similar storage capacities for Na- and Li-ions at relatively low current rates (i.e. C/10). Interestingly, *operando* X-ray diffraction shows that insertion of Na-ions induces a solid solution transition in the crystalline $Fe_{1.13}(PO_4)(OH)_{0.39}(H_2O)_{0.61}$ end-member simultaneously with a major amorphization. This result adds to the series of observation of phosphate-based materials undergoing order-disorder transitions during Na-ion storage. $Fe_{1.13}(PO_4)(OH)_{0.39}(H_2O)_{0.61}$ is thus ideal for enhancing our knowledge on such phenomena. To this end, using total X-ray scattering with pair distribution function analysis, we show that the amorphous phase is Na-rich $Na_xFe_{1.13}(PO_4)(OH)_{0.39}(H_2O)_{0.61}$ with the local $[FeO_6]$-$[PO_4]$ motif retained but coherence lengths of only ca. 0.6 nm. Our investigation also reveals that the crystallinity of $Fe_{1.13}(PO_4)(OH)_{0.39}(H_2O)_{0.61}$ is regained upon Na-extraction (battery recharge), i.e. the order-disorder transition is reversible.

Introduction

In rechargeable batteries, the electrodes are typically composed of crystalline materials. On the cathode (positive) side, the electrodes are most often transition metal oxides or phosphates.[1-3] The process of battery charge and discharge, i.e. ion-extraction and -intercalation leads to a phase transition between the reduced and oxidized form of the cathode (i.e. the Li-rich and Li-poor phases in a Li-ion battery), which brings about either an isomorphic or polymorphic structural transformation. The structural evolution of this process has been studied for a wide range of electrode materials.[4] In most cases, the structural transitions have been studied from a purely crystalline perspective, i.e. as transitions between two crystalline phases. However, recent studies have revealed formation of nano crystalline or amorphous phases, which form either as intermediates or as the fully oxidized/reduced product.[5-12] It is worth to notice that several reports of such order-disorder transitions involve Na-ion storage in phosphate-based materials.[5,7,12] It has been suspected that the disorder is induced by the larger strain accompanying intercalation of the significantly larger Na-ion (102 pm) compared to the Li-ion (72 pm).[5]

The interest in Na-ion batteries is constantly increasing due to the low cost and high abundance of sodium, which makes the technology a highly interesting alternative to the Li-ion battery. Furthermore, Na has a suitable redox potential of $E°_{Na+/Na} = -2.71$ V versus the standard hydrogen electrode, which is only 0.3 V above that of Li^+/Li.[1,2] An additional advantage of the Na-ion technology is that many Li-ion electrode materials also allow efficient intercalation of Na-ions.[13-16] However, there is still a great need for deeper insight into the effects of exchanging intercalation of Li-ions with Na-ions – both when it comes to electrochemical performance, structural changes and battery stability.

We have for the first time investigated Lipscombite iron(III) hydroxide phosphate hydrate $Fe_{2-y}(PO_4)(OH)_{3-3y}(H_2O)_{3y-2}$ (y = 0.87) as a Na-ion battery cathode material. We found that Na-ion insertion into the crystalline $Fe_{2-y}(PO_4)(OH)_{3-3y}(H_2O)_{3y-2}$ framework induces severe reversible amorphization. Thus, the material is ideal as a model material for increasing our knowledge of reversible order-disorder transitions induced by ion-storage. Lipscombite $Fe_{2-y}(PO_4)(OH)_{3-3y}(H_2O)_{3y-2}$ has previously received attention as Li-ion battery cathode mainly due to its potentially low production cost and the fact that it stores Li-ion reversibly (>100 mAh/g) via a complete solid solution reaction.[17-23] The crystalline tetragonal lipscombite structure (space group $I4_1/amd$), is built from chains of face-sharing $[FeO_6]$ octahedra aligned along the *a*- and *b*-axis in alternating layers. The phosphate groups interconnect the $[FeO_6]$ chains via corner sharing. The hydroxide/water is situated on the corners of the $[FeO_6]$ octahedra (Figure 1). Note that a significant amount of vacancies are found on the Fe-position, i.e. taking charge neutrality into account, the general composition is $Fe_{2-y}\square_y(PO_4)(OH)_{3-3y}(H_2O)_{3y-2}$. Reported Fe-occupancy (y) ranges from 1.18 to 1.39.[17-23]

In this study, we investigate the electrochemical behavior of $Fe_{1.13}(PO_4)(OH)_{0.39}(H_2O)_{0.61}$ (henceforth denoted FPOH) as a cathode for Na-ion batteries by examining the electrochemical behavior, and most importantly, we study the structural transformation induced by Na-ion intercalation and extraction by *operando* powder X-ray diffraction (PXRD) and *ex situ* total X-ray scattering (TXS) with pair distribution function (PDF) analysis. The complementarity of PXRD

---

[a] Department of Physics, Chemistry and Pharmacy, University of Southern Denmark, Campusvej 55, 5230 Odense M, Denmark.

Electronic Supplementary Information (ESI) available: Results of Rietveld refinement of the PXRD data for the pristine material, Results of the PDF data for the pristine, discharged and recharged electrode, Rate capability tests of FPOH vs. Li and Na, Scale factor of Na_xFPOH as a function of Na-content, PDF data for crystalline as-synthesized FPOH with correlations assigned to specific interatomic distances, PDF data for amorphous $Na_{0.88}FPOH$ (discharged state) with calculated contributions for the individual phases.

and TXS allows us to gain insight into the structural nature of both the crystalline and amorphous parts of the active cathode material.

Experimental

All sample handling and battery fabrication was performed in an Ar-filled MBraun glovebox equipped with circulation purifier (O_2 < 1 ppm, H_2O < 0.1 ppm).

Synthesis of $Fe_{2-y}(PO_4)(OH)_{3-3y}(H_2O)_{3y-2}$

FPOH was prepared by hydrothermal synthesis. Aqueous solutions of $FeCl_3$ (97 %, Aldrich) and Na_3PO_4 (96 %, Aldrich) were mixed with cetyltrimethylammonium bromide powder (CTAB, ≥ 99 %, Aldrich) to form a total volume of 42.5 mL in a 1:1:0.87 molar ratio. The solution was transferred to an 85 mL Teflon cup which was sealed in a stainless-steel autoclave and heated at 150 °C for 3 hours.

Elemental Analysis by Inductively Coupled Plasma-Optical Emission Spectrometry

The elemental ratio between Fe and P was determined using a PerkinElmer Inductively Coupled Plasma-Optical Emission Spectrometer (ICP-OES) after dissolution of a ~0.1 g sample in concentrated nitric acid (≥ 65 %).

Electrochemical characterization

For electrochemical characterization, the as-prepared material was mixed with carbon black (CABOT VXC72), graphite (C-nergy SFG 6 L, Imerys) and Kynar binder (HSC900 PVDF, MTI Corporation) in a 75: 10:10:5 mass ratio and suspended in N-methyl-2-pyrrolidone (NMP, 99.5 %, Sigma-Aldrich). The slurry was coated onto aluminum foil (0.05 mm thickness). After drying, the coating was scraped off the Al-foil, and the composite powder was pressed into a free-standing pellet at 1.8 -2.0 ton (o.d. 7 mm, thickness: ca. 140 µm, and mass: ca. 9 mg). For the *operando* PXRD measurement, the mass of the free-standing pellet was ca. 10 mg.

Galvanostatic cycling and cyclic voltammetry (CV) were performed in a two-electrode ½-in. Swagelok-type cell, using hand-rolled Na-ion metal (99.9 %, Aldrich) as anode and eight drops of 1 M NaTFSI in ethylene carbonate/dimethylcarbonate (EC:DMC = 1:1 v/v, 99.9 %, Solvionic) as electrolyte. The two electrodes were separated by a microporous glass fiber separator (Wattman GF/B). For the Galvanostatic cycling, cells were cycled at C/10-rate between 1.5 and 4.2 V. For CV, the same potential limits were used with a sweep rate of 0.05 mV/s.

To obtain samples for *ex situ* pair distribution analysis, two battery cells with free standing pellets were assembled. One was discharged at C/10 to 1.5V after which the potential was kept at 1.5V for 5 hours. The second cell was taken through a discharged to 1.5 V and charged to 4.2 V, where after the potential was fixed at 4.2 V for 5 hours. The pellets were removed from the cells and washed with EC:DMC inside the glovebox.

Synchrotron radiation powder X-ray diffraction and total scattering

Synchrotron radiation powder X-ray diffraction (SR-PXRD) and total X-ray scattering (TXS) for PDF analysis were obtained at beamline 11-ID-B at the Advanced Photon Source, Advanced National Laboratory using an X-ray wavelength of 0.2113 Å and a PerkinElmer amorphous silicon 2D detector. For *ex situ* measurements, samples were mounted in polyimide capillaries (0.0435” OD and 0.0395” ID, Cole-Parmer). For *operando* measurements, the electrode pellet was mounted in an AMPIX-type battery test cells[24] specially designed for *operando* battery-scattering measurements using the same cell-stack configuration as for the electrochemical characterization. The collected two-dimensional data were processed with the Fit2D program.[25] All patterns (PXRD and TS separately) were scaled to compensate for beam intensity fluctuations using the intensity of the primary beam shoulder average over a 2θ- or Q-range at small angles.

Rietveld refinement of PXRD data

Rietveld refinement of the PXRD data was performed using the Fullprof software.[26] The background was described by linear interpolation between manually selected points. The diffraction peaks were described using a Pseudo-Voigt profile function. Generally, the unit cell parameters, profile parameters, atomic positions and isotropic vibration factors were refined. The refinement of the *operando* data was performed using the sequential refinement option in Fullprof. For these, the isotropic vibration factors were fixed and instead the overall vibration factor was refined.

Refinement of the pair distribution functions

The TXS data were treated using the PDFgetX3 software[27] to obtain PDFs. The r_{poly} value was set to 0.9 Å and an upper Q-range cutoffs ($Q_{maxinstrument}$) of 24 $Å^{-1}$ were used. The PDFs were fitted in real space using the PDFgui software.[28] Instrumental broadening parameters, Q_{damp} and Q_{broad} were determined by fitting the PDF of the standard CeO_2 yielding values of about 0.03 and 0.009, respectively. For the refinement of the FPOH phases, the scale factors, the unit cell parameters, atomic displacement parameters, delta2 and the sp-diameter were refined. For the discharged and recharged samples, a local graphite phase was added in order to account for the conductive carbon and binder added to the sample. The details of the PDF refinement results are given in Tables S2-S4.

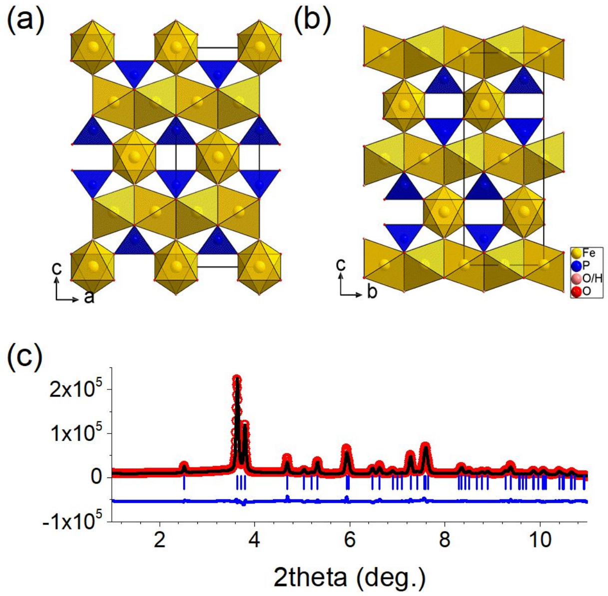

Figure 1. (a and b) Crystal structure of lipscombite iron(III) hydroxide phosphate, $Fe_{2-y}(PO_4)(OH)_{3-3y}(H_2O)_{3y-2}$ (space group $I4_1/amd$) shown along the *b*- and a-axis, respectively. (c) Rietveld refinement profile of *ex situ* PXRD data (λ = 0.2113 Å, beamline 11-ID-B at the Advanced Photon Source) of the as-synthesized $Fe_{1.13}(PO_4)(OH)_{0.39}(H_2O)_{0.61}$ (R_{Bragg} = 6.61%).

Results and discussion

The hydrothermally prepared $Fe_{2-y}(PO_4)(OH)_{3-3y}(H_2O)_{3y-2}$ crystalizes as expected in the tetragonal lipscombite structure

(Figure 1) with space group *I*4_1/*amd* (COD: 7001236) and unit cell parameters *a* = 5.1702(4) and *c* = 13.0600(14) Å obtained from Rietveld refinement (see further details in Table S1, supplementary information). From ICP-OES the Fe-content is determined to 1.13(2) per formula unit, which brings the composition to $Fe_{1.13}(PO_4)(OH)_{0.39}(H_2O)_{0.61}$. Rietveld refinement of the Fe-occupancy agrees well suggesting a Fe-content of 1.13(4) per unit cell, which is in line with no impurities being observed by PXRD (or by PDF analysis, see below). The composition $Fe_{1.13}(PO_4)(OH)_{0.39}(H_2O)_{0.61}$ will be referred to as FPOH in the following. Scherrer analysis using the (103)-reflection (3.63° 2θ) reveals that the crystallite of the as-synthesized material is 32(2) nm (taking instrumental broadening into account). In a previous study (see ref. 23), we completed a thorough characterization of the starting material using scanning electron microscopy. This revealed that the crystallites are arranged in agglomerates of spherical particles with an approximate particle size of 2−6 µm in diameter.[23]

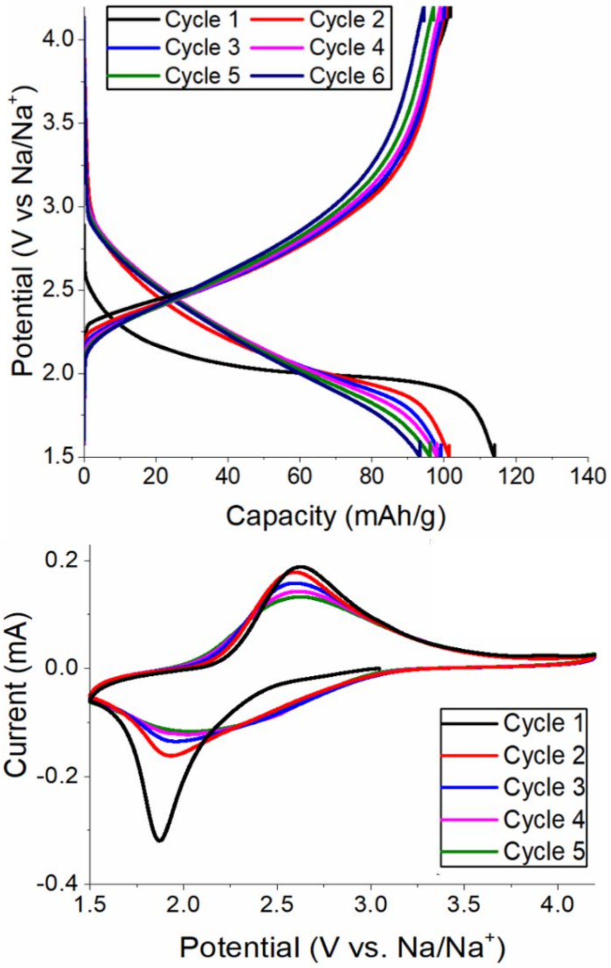

Figure 2. (Top) Galvanostatic capacity-potential profile (C/10 current rate) and (bottom) cyclic voltammogram (sweep rate = 0.05 mV/s) for $Fe_{1.13}(PO_4)(OH)_{0.39}(H_2O)_{0.61}$ cycled vs. Na.

Galvanostatic discharge-charge cycling of FPOH vs. Na yields a discharge capacity of 114 mAh/g during the first discharge, which corresponds to intercalation of 0.73Na (Figure 2). The potential profile is sloped indicative of the Na-ions being intercalated through a solid solution transformation in a similar manner as observed for Li-ion intercalation.[23] The potential hysteresis in the first cycle is ca. 0.7 V, while it drops to ca. 0.55 V in subsequent cycles. Between the first and second discharge 12.5 mAh/g is lost, after which ca. 2 % capacity is lost per cycle. It is worth to notice that at low current rates (C/10), the Na-ion storage capacity of the material is similar to the Li-ion storage capacity. However, at higher current rates, FPOH provides significantly lower capacities vs. Na than vs. Li, i.e. <20 mAh/g is obtained at 1C discharge vs. Na, while ca. 50 mAh/g is obtained vs. Li at 1C (see Figure S1). This points to a severe kinetic limitation for Na-ion storage in this material, which is also underlined by the potential hysteresis during Na-ion storage (0.55 V) being significantly higher than during Li-ion storage (0.21 V).[23]

To obtain further insight into the redox processes, cyclic voltammetry was performed on FPOH against Na (Figure 2). During Na-insertion (Fe(III) reduction), an intense cathodic current is observed at 1.87 V. With repeated cycling the current peak broadens, and the intensity decreases simultaneously with a shift to higher potentials. During the first Na-extraction, the anodic current peaks at 2.63 V. The peak potential is relatively constant over five cycles. However, repeated cycling leads to increased broadening of the anodic currents. Overall, for the second cycle and onwards, the broad peaks of the voltammogram are indicative of solid solution behaviour. In line with the galvanostatic cycling, the polarization decreases with repeated cycling mainly due to a shift in the Na-insertion (Fe(III) reduction) potential). After five cycles the polarization converges at about 0.6 V.

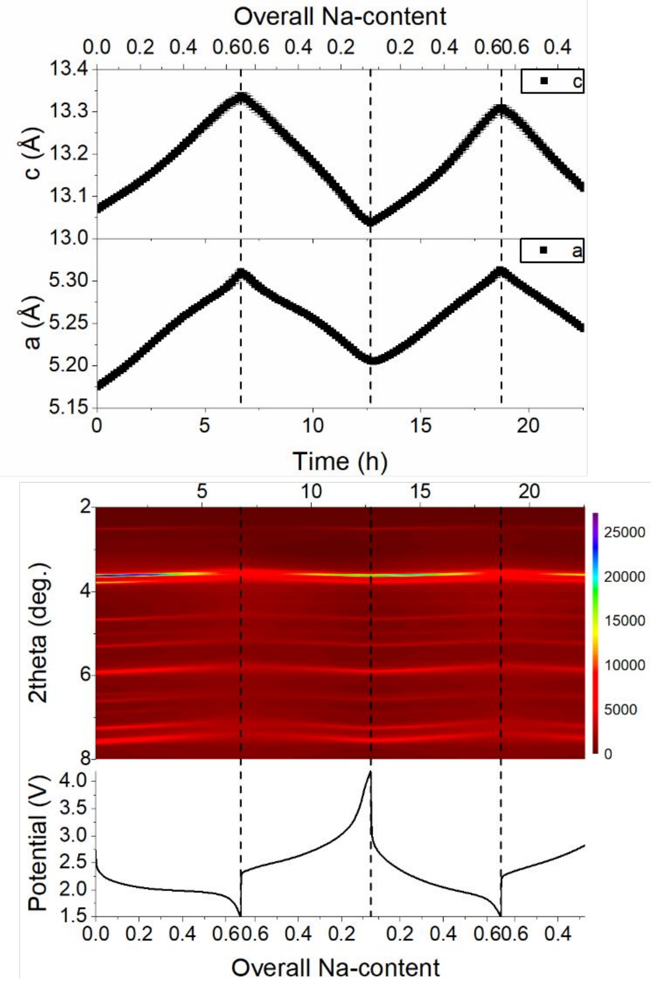

Figure 3. Results of *operando* powder X-ray diffraction measurements during discharge and charge of $Fe_{1.13}(PO_4)(OH)_{0.39}(H_2O)_{0.61}$ cycled vs. Na. (Bottom) Galvanostatic composition-potential profile (C/10 rate) with (middle) simultaneously collected *operando* PXRD data (λ = 0.2113 Å, beamline 11-ID-B at the Advanced Photon Source) and (top) unit cell parameters for the crystalline Na_xFPOH extracted by Rietveld refinement.

The structural evolution during Na-insertion and -extraction, i.e. discharge and charge, were probed using *operando* PXRD (Figure 3). As expected, the unit cell expands and contracts during discharge and charge, respectively. This is a natural effect of both the change in Fe-oxidation state (which changes the ionic radius) and the intercalation of the relatively large Na-ions. The Bragg reflections and therefore also the lattice parameters change continuously throughout the galvanostatic experiment confirming that Na-ion intercalation occurs through a solid solution reaction with formation of Na$_x$FPOH. Rietveld refinement of the unit cell parameters of Na$_x$FPOH reveals that the unit cell parameters expand and contract almost linearly with respect to the Na-content. The unit cell volume expands 7.46 vol% during the first discharge and contracts again by 6.08 % during the first charge. The overall Na-content corresponds well with the unit cell expansion and contraction providing a relatively constant ratio between the unit cell volume and overall Na-content. Some anisotropy is however observed for the unit cell parameters during the first cycle (Table 1). The *a*- and *c*-axis expands 2.61 and 2.06 %, respectively, during the first discharge. In the first charge, the *a*-axis contracts only by 1.98 %, while the *c*-axis contracts by 2.25 %. Hence, after recharge, the *a*-axis is larger than initially while the *c*-axis is smaller. During the second discharge the expansion appears to be isotropic. Hence, the first reduction-oxidation cycle appears to induce a small anisotropic change in the crystalline structure. Even though, the overall change in unit cell parameters during Li-ion storage are smaller (in line with the Li-ion being smaller), the anisotropic behavior is still prevalent. Thus, the anisotropy may be an inherent property of the FPOH structure. The effect may be linked to reduction of the crystal water as suggested in previous studies.[17,18] It is also worth to note that the intercalation positions of neither Li- nor Na-ions in the FPOH structure is known and that the interaction of the ions with the FPOH lattice may also cause an anisotropy in the unit cell parameters. Most likely the ions are stored in the vacant interstitial sites in the channels in the [100] and [010] direction along the face-sharing [FeO$_6$]-chains. This could indeed lead to decreased repulsion along the *c*-axis and thereby increase the contraction in this direction. The vacant Fe-sites (estimated size 0.64 Å) are also a possibility for Li-ion intercalation,[29] however, the larger Na-ions will likely not fit into these sites.

Table 1. Linear and volume change during Na-insertion (discharge) and -extraction (charge) in crystalline Fe$_{2-y}$(PO$_4$)(OH)$_{3-3y}$(H$_2$O)$_{3y-2}$

	1st discharge	1st charge	2nd discharge
Δa [%]	2.61	-1.98	2.06
Δc [%]	2.06	-2.25	2.09
Δvol [%]	7.46	-6.08	6.34
Overall Na-content	0.667	0.065	0.663

In the *operando* PXRD data, it is notable that after insertion of ca. 0.4Na, the Bragg reflections of FPOH begin to gradually weaken in intensity. At the end of discharge, only ca. 65 % of the initial reflected integrated peak intensity from Na$_x$FPOH is left and the reflections have broadened significantly (Figure S2 and Figure 4). Scherrer analysis based on the Na$_x$FPOH Bragg reflections at the end of the 1st discharge reveals that the average crystallite size has decreased to 6(2) nm. Interestingly, upon recharge 80 % of the FPOH Bragg intensity is regained and the crystallite size increases to 29(2) nm suggesting that Na-ion intercalation during discharge induces a reversible order-disorder transition with formation of an amorphous Na-rich FPOH phase in the discharged state. We note that this also occurs during the second cycle. A similar effect was observed during Li-ion storage in FPOH, however to a much smaller extent as only ca. 20 % of the diffracted intensity was lost.[23]

To obtain details about the structure of the amorphous phase, total X-ray scattering (TXS) data was collected for three samples: As-synthesized FPOH, the Na-rich electrode at the end of discharge (Na$_{0.83}$FPOH) and the Na-poor electrode at the end of recharge (Na$_{0.02}$FPOH) (Figure 5). The crystalline structure obtained from Rietveld refinement of the as-synthesized FPOH explains the PDF well and yields results like those obtained from the PXRD analysis (see Table S1, S2 and Figure S2).

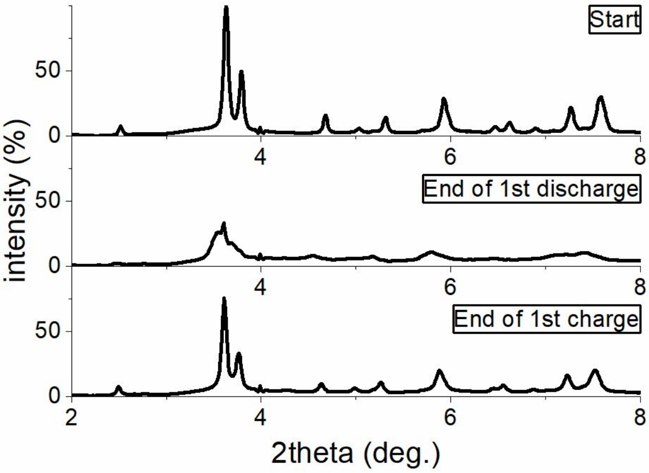

Figure 4. Selected *operando* PXRD data (λ = 0.2113 Å, beamline 11-ID-B at the Advanced Photon Source) of (top) Fe$_{1.13}$(PO$_4$)(OH)$_{0.39}$(H$_2$O)$_{0.61}$ (FPOH), (middle) Na$_{0.83}$FPOH obtained by discharging the FPOH electrode vs. Na at C/10-rate and (bottom) Na$_{0\cdot02}$FPOH obtained by taking the FPOH electrode through a complete discharge-charge cycle at C/10-rate.

The PDF for Na$_{0.83}$FPOH (Na-content based on the electrochemical data) obtained after battery charge is markedly different from the as-synthesized material: Not only have the peak positions generally changed but the well-defined correlations also die out at much lower *r*, i.e. no well-defined peaks are observed at *r* > 28 Å in line with the low range of order expected in this state. The PDF of Na$_{0.83}$FPOH can be described by a two-phase model employing a local Na$_x$FPOH phase and a small amount of the crystalline Na$_x$FPOH phase as obtained from Rietveld refinement of the *operando* PXRD data at the end of discharge. For the local Na$_x$FPOH phase, the crystalline Na$_x$FPOH was used as starting model and all unit cell parameters, the correlated atomic vibrations (δ_2) and the coherent domain size (sp-diameter) were freely refined (Table S3). From the refinement of the PDF, it is clear that the local Na$_x$FPOH constitutes the majority of the electrode as the scale factor for the local Na$_x$FPOH is more than five times larger than that for the crystalline Na$_x$FPOH. Thus, the PDF cannot be satisfactorily fitted without employing this local phase (see also Figure S3). However, the fact that the crystalline Na$_x$FPOH can be used as a starting model for the local phase proves the structural similarities between these phases. We do note that in neither the local nor crystalline Na$_x$FPOH phase, Na-ions were added to the structure as the positions of these are presently unknown. As no distinct PDF correlations are left unexplained in the PDF fit at r-values matching possible Na-O or Na-Fe interatomic distances, the decision was made not to attempt to include Na in the structures. The fact that no clear Na-O or Na-Fe interatomic distances are observed in the data, could suggest that Na is not arranged in a highly ordered manner in the FPOH structure.

Refinement of the unit cell parameters for the local Na$_x$FPOH phase shows a clear preference for maintaining two short lattice parameters of equal size and a third longer lattice parameters, i.e. the tetragonal cell is maintained. The short lattice parameters (the *a*- and *b*-axis) are somewhat longer for the local Na$_x$FPOH (5.56 Å) than for the crystalline Na$_x$FPOH (5.27 Å), which may be explained by a higher amount of Na in this phase or in other words a lower average oxidation state providing a larger average ionic radius for Fe. The third lattice parameter (the *c*-axis) is on the other hand significantly shorter for the local Na$_x$FPOH phase (10.82 Å) than for the crystalline phase (13.11 Å). The contraction along the c-axis may be a result of a high degree of Na-ion filling in the channels in the [100] and [010] directions, which may minimize electrostatic repulsion between the [PO$_4$]-anions. Relating the Lipscombite structure to the changes in unit cell parameters suggests that the chains of face-sharing [FeO$_6$] octahedra aligned along the *a*- and *b*-axis remains somewhat intact in the local Na$_x$FPOH phase. In contrast, the stacking of the chains along the *c*-axis appears to be significantly different from the crystalline state. This is reasonable considering the connectivity between chains along the *c*-axis is mainly via corner-connectivity, which has a higher structural flexibility and may also have a higher affinity for disordering.[30]

The coherence length extracted from refinement of the PDF (the sp-diameter), i.e. the extent of the structural order in the local Na$_x$FPOH phase is only ca. 0.6 nm. Hence, the local Na$_x$FPOH phase can truly be considered an amorphous phase in agreement with no Bragg reflections being observed for this phase. The coherence length corresponds roughly to the motif of 2-3 face-sharing [FeO$_6$] connected via the corners to a [PO$_4$]-tetrahedra and to two face sharing [FeO$_6$]-octahedra in another (orthogonal) [FeO$_6$]-chain (Figure 6). The coherence length for the crystalline Na$_x$FPOH phase is approximately 10 times larger (i.e. 5.3 nm), which is in agreement with the Scherrer analysis and with this phase being observed as broad Bragg reflections in the diffraction data. The coherence length of the crystalline Na$_x$FPOH phase corresponds to ca. 10 unit cells along the *a*- and *b*-axis and ca. 4 unit cells along the *c*-axis.

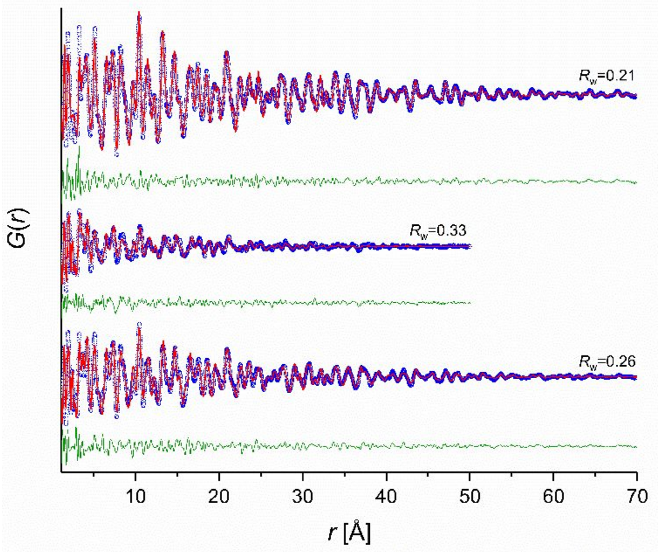

Figure 5. Pair distribution functions obtained from ex situ total X-ray scattering data of (top) as-synthesized $Fe_{1.13}(PO_4)(OH)_{0.39}(H_2O)_{0.61}$ (FPOH), (middle) Na$_{0.83}$FPOH obtained by discharging the FPOH electrode vs. Na at C/10-rate and (bottom) Na$_{0\text{-}02}$FPOH obtained by taking the FPOH electrode through a complete discharge-charge cycle at C/10-rate. Observed PDFs are in blue, calculated PDFs in red, and difference curves in green.

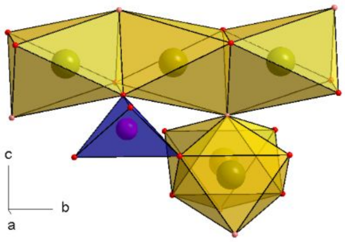

Figure 6. The structural motif of the local (amorphous) Na$_x$FPOH phase as observed by PDF at the end of the 1st discharge ([FeO$_6$] in yellow, [PO$_4$] in blue). The diameter of the motif (ca. 0.6 nm) is based on the coherence length, i.e. the sp-diameter obtained from refinement of the PDF (Figure 5, middle).

The PDF of the recharged sample with global composition Na$_{0.02}$FPOH (based on the electrochemical data) can be fitted using the crystalline FPOH structure of the pristine material and a local FPOH phase (Figure 5, bottom). As mentioned, it is evident from the *operando* PXRD data that crystalline Na$_x$FPOH reforms upon recharge, i.e. the scale factor extracted from Rietveld refinement increases to 81 % of the original value. This is corroborated by the PDF analysis. Furthermore, the domain size of the crystalline FPOH increases to 12 nm as compared to the 5 nm in the discharged sample. In the as-synthesized material, a domain size of 14 nm was obtained from PDF analysis. This clearly shows that the crystalline Na$_x$FPOH phase has been reconstructed from the amorphous Na$_x$FPOH phase during extraction of the Na-ions. This is also clearly evidenced from the reappearance of sharp Bragg reflections in the diffraction data.

Thus, the phase transition between the crystalline and amorphous phase is partly reversible and is most probably driven by intercalation of the relatively large Na-ion inducing a severe strain on the crystalline structure. The fact that a similarly pronounced amorphization was not observed in previous studies of Li-ion intercalation in FPOH can likely be explained by the smaller size of the Li-ion and that these may also enter the vacant Fe-sites in the [FeO$_6$]-chains. All Na-ions, occupying the space in the channels in the [100] and [010] directions, may cause increased ionic repulsion as the Na-content increases during discharge, which may induce amorphization. Whether the phase transition between the crystalline and amorphous phase occurs via a two-phase transitions or solid solution reaction is still not clear. Judging purely on the scale factor of the crystalline Na$_x$FPOH (Figure S2) suggest that the phase evolution differs between charge and discharge, as the scale factor of crystalline Na$_x$FPOH decreases continuously during all of discharge, while it remains constant for the initial part of the charge. The origin of this behavior awaits further *operando* PDF investigations.

Conclusions

Nanoscale FPOH provides a Na-ion storage capacity of ~100 mAh/g at a current rate of C/10, which is similar to the capabilities of the material toward Li-ion storage. At a first glance, crystalline FPOH intercalates Na-ions reversibly via a simple solid solution reaction albeit some lattice anisotropy is observed, which may be subscribed to reduction of crystal water. Interestingly, a major decrease in the diffracted intensity from Na_xFPOH is observed in the *operando* PXRD data during discharge. This is caused by a severe amorphization induced by the ion-intercalation/reduction. Using PDF analysis, we showed that the amorphous phase is built from a structural motif resembling the crystalline Na_xFPOH structure. However, the coherence length of the amorphous state extents only to ca. 6 nm. The order-disorder transition is partly reversible with the crystalline FPOH reforming upon recharge (Na-ion extraction).

Conflicts of interest

There are no conflicts to declare.

Acknowledgements

We thank the Independent Research Fund Denmark, (Grant no. 4184-00143A) and the Carlsberg Foundation (Grant no. CF17-0823) for funding this research. Danscatt is acknowledged for funding travel costs related to the synchrotron experiments. We used resources of the Advanced Photon Source at Argonne National Laboratory (under Contract No. DE-AC02-06CH11357). Special thanks to Dr. Olaf J. Borkiewicz and Dr. Kamila M. Wiaderek at beamline 11-ID-B, Advanced Photon Source for experimental support.

References

1 C. Vaalma, D. Buchholz, M. Weil, S. Passerini, *Nat. Rev.*, 2018, **3**, 18013
2 J.-Y. Hwang, S.-T. Myung, Y.-K. Sun, *Chem. Soc. Rev.*, 2017, **46**, 3529-3614
3 M. Rosa Palacin, *Chem. Soc. Rev.*, 2009, **38**, 2565–2575
4 D. Liu, Z. Shadike, R. Lin, K. Qian, H. Li, K. Li, S. Wang, Q. Yu, M. Liu, S. Ganapathy, X. Qin, Q.-H. Yang, M. Wagemaker, F. Kang, X.-Q. Yang, B. Li, *Adv. Mater.*, 2019, *31*, 1806620
5 K. Xiang, W. Xing, D. B. Ravnsbæk, L. Hong, M. Tang, Z. Li, K. M. Wiaderek, O. J. Borkiewicz, K. W. Chapman, P. J. Chupas, Y.-M. Chiang, *Nano Lett.*, 2017, **17**, 1696-1702
6 F. Jiao, P. G. Bruce, *Adv. Mater.*, 2007, **19**, 657–660.
7 J. Billaud, R. J. Clément, A. R. Armstrong, J. Canales-Vázquez, P. Rozier, C. P. Grey, P. G. Bruce, *J. Am. Chem. Soc.*, 2014, **136**, 17243−17248.
8 V. Pralong, V. Gopal, V. Caignaert, V. Duffort, B. Raveau, *Chem. Mater.*, 2012, **24**, 12−14.
9 M. Freire, O. I. Lebedev, A. Maignan, C. Jordy, V. Pralong, *J. Mater. Chem. A*, 2017, **5**, 21898–21902.
10 C. K. Christensen, M. A. Hasen Mamakhel, B. B. Iversen, A. R. Balakrishna, Y.-M. Chiang, D. B. Ravnsbæk, *Nanoscale*, 2019, **11**, 12347-12357.
11 C. K. Christensen, D. R. Sørensen, J. Hvam, D. B. Ravnsbæk, *Chem. Mater.*, 2019, **31**, 295-562
12 A. Nassiri, N. Sabia, A. Sarapulov, M. Dahbi, S. Indris, Helmut Ehrenberg, Ismael Saadoune, *J. Power Sources*, 2019, **418**, 211–217.
13 X. D. Xiang, K. Zhang, J. Chen, *Adv. Mater.* 2015, **27**, 5343-5364
14 C. Delmas, *Adv. Energy Mater.* 2018, **8**, 1-9
15 M. I. Jamesh, A. S. Prakash, *Journal of Power Sources* 2018, *378*, 268-300
16 P. K. Nayak, L. T. Yang, W. Brehm, P. Adelhelm, *Angew. Chem.-Int. Edit.* 2018, *57*, 102-120.
17 M. Dolle, S. Patoux, T. J. Richardson, *Journal of Power Sources* **2005**, *144*, 208-213
18 Y. N. Song, P. Y. Zavalij, N. A. Chernova, M. S. Whittingham, *Chemistry of Materials* **2005**, *17*, 1139-1147
19 S. M. Zhang, J. X. Zhang, S. J. Xu, X. J. Yuan, T. Tan, *Journal of Power Sources* **2013**, *243*, 274-279
20 M. S. Whittingham, Y. N. Song, S. Lutta, P. Y. Zavalij, N. A. Chernova, *Journal of Materials Chemistry* **2005**, *15*, 3362-3379
21 Y. Song, P. Y. Zavalij, M. S. Whittingham, in *Solid State Ionics-2002, Vol. 756* (Eds.: P. Knauth, J. M. Tarascon, E. Traversa, H. L. Tuller), **2003**, pp. 249-253
22 Z. L. Wang, S. R. Sun, F. Li, G. Chen, D. G. Xia, T. Zhao, W. S. Chu, Z. Y. Wu, *Materials Chemistry and Physics* **2010**, *123*, 28-34
23 C. Henriksen, C. Wegeberg, D. B. Ravnsbæk, *J. Phys. Chem. C* **2018**, *122*, 1930-1938.
24 O. J. Borkiewicz, B. Shyam, K. M. Wiaderek, C. Kurtz, P. J. Chupas and K. W. Chapman, J. Appl. Crystallogr., 2012, 45, 1261–1269
25 A. P. Hammersley, S. O. Svensson, M. Hanfland, A. N. Fitch, D. Hausermann, High Pressure Res., 1996, 14, 235–248.
26 J. Rodriguezcarvajal, Phys. B 1993, 192, 55−69.
27 P. Juhás, T. Davis, C. L. Farrow and S. J. L. Billinge, J. Appl. Crystallogr., 2013, 46, 560–566.
28 C. L. Farrow, P. Juhas, J. W. Liu, D. Bryndin, E. S. Božin, J. Bloch, T. Proffen and S. J. L. Billinge, J. Phys.: Condens. Matter, 2007, 19, 335219.
29 A. Mahmoud, C. Karegeya, M. T. Sougrati, J. Bodart, B. Vertruyen, R. Cloots, P. E. Lippens, F. Boschini, *Acs Applied Materials & Interfaces* 2018, **10**, 34202-34211.
30 W. H. Zachariasen, *J. Amer. Chem. Soc.* 1932, **54**, 3841-3851.

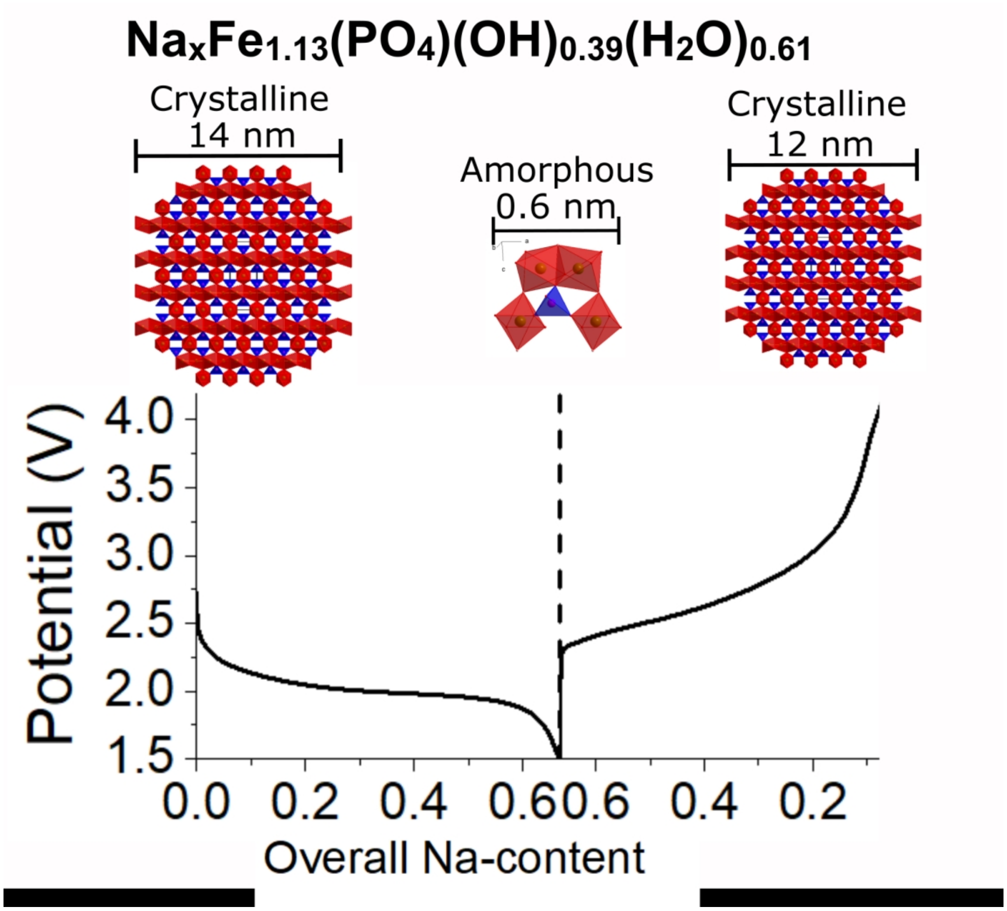
$Na_xFe_{1.13}(PO_4)(OH)_{0.39}(H_2O)_{0.61}$
Crystalline
14 nm
Amorphous
0.6 nm
Crystalline
12 nm
Potential (V)
4.0
3.5
3.0
2.5
2.0
1.5
0.0
0.2
0.4
0.6
0.6
0.4
0.2
Overall Na-content